Use of the Sentinel-1 Satellite Data in the SNAP Platform and the WebGNOME Simulation Model for Change Detection Analyses on the Persian Gulf Oil Spill

Giacomo Caporusso(✉), Marino Dell'Olio, and Eufemia Tarantino

Department of Civil, Environmental, Land, Construction and Chemistry (DICATECh), Politecnico di Bari, Via Orabona 4, 70125 Bari, Italy
giacomo.caporusso@poliba.it

Abstract. Oil spills in the marine environment increasingly represent a significant problem for the ecosystem. The intensification of the operations of extraction, transport and storage of hydrocarbons has in fact caused a greater frequency of the occurrence of accidents, with consequent dispersion of the material in an uncontrolled manner. Remote sensing plays a fundamental role in identifying and monitoring these phenomena. In particular, using satellite images obtained with Synthetic Aperture Radar (SAR) technology, spill recognition methodologies have been developed through automatic and semi-automatic approaches. This paper analyses the accident that occurred in March 2017 in the Persian Gulf, through the Sentinel-1 Single Look Complex (SLC) and Ground Range Detected (GRD) SAR image Change Detection technique, to evaluate the dispersion of hydrocarbons. The use of the SentiNel Application Platform (SNAP) software of the European Space Agency (ESA) made it possible to determine the amount of oil involved in the spill. Furthermore, through the Web-based application General NOAA Oil Modeling Environment (WebGNOME) the dynamic propagation model of the spilled hydrocarbons was produced based on the morphology and meteorological conditions of the site examined which further confirmed the validity of the Change Detection operations Sentinel-1 images. Finally, the results were compared with those obtained using automatic methodologies developed by ESA, confirming the greater accuracy of the procedures used in this study.

Keywords: Oil spill · Marine pollution · SAR · Sentinel-1 · SNAP · WebGNOME · Persian gulf

1 Introduction

Since 1990 there have been over 170 large-scale accidents involving tankers, bulk carriers, Floating Production Storage and Offloading (FPSO) and barges which, accidentally, caused the spill of hydrocarbons. In 2021 alone, losses totalling over 10,000 tons of hydrocarbons were recorded [1, 2]. The introduction of remote sensing techniques has

© The Author(s), under exclusive license to Springer Nature Switzerland AG 2022
O. Gervasi et al. (Eds.): ICCSA 2022 Workshops, LNCS 13379, pp. 369–386, 2022.
https://doi.org/10.1007/978-3-031-10545-6_26

favoured a rapid and incontrovertible development in the study and monitoring of hydrocarbon spills, especially those that occur daily in the marine environment, in terms of quality and quantity of data deductible from analysis of satellite images [3]. The most widely used method for data acquisition involves the use of Aerial Photogrammetry, Unmanned Aerial Vehicle (UAV) [4–6] or satellites, especially those equipped with SAR sensors [7]. The diffusion of petroleum materials on an aqueous surface constitutes a large floating film, obviously different in terms of the chemical nature and roughness of the surrounding water surface. These characteristics determine a different ability to reflect the radar beam, determining a reduction in the backscatter detected by the instrument. Moreover, the SAR image is, thanks to the radar-type sensor, more efficient in the context of Oil Spill detection than that of a multi-spectral nature, as it is independent of lighting, cloudiness and other weather conditions that often negatively affect the quality of other types of satellite images [7]. For these reasons it was considered appropriate to analyse the oil spill that occurred off the coast of Dubai in March 2017 through Sentinel-1 images concomitant with the event. The work carried out has the following objectives ì) to compare the volume of floating hydrocarbons derived from the analysis of a single image with that derived from the Change Detection between the image acquired previously and that in conjunction with the SNAP event; ii) evaluate the effectiveness of a statistical approach in defining the backscatter value that allows you to distinguish water from oil; ìíì) evaluate the behaviour of the Coherence interferometric parameter. Finally, the analysis performed was compared with the outputs produced by the Web General NOAA oil modeling environment (WebGNOME), a web application developed by NOAA [8]. This tool, starting from the data relating to the surrounding conditions of the environment and the event, allowed both to reconstruct the dynamics of the spill and to trace the quantities of hydrocarbons released into the environment.

2 Materials and Methods

2.1 Study Area

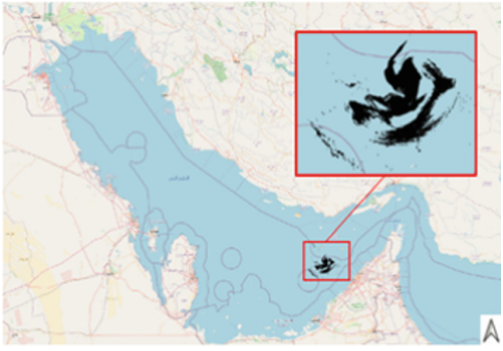


Fig. 1. Area affected by the spill. General Scale 1:10.000.000. Detail Scale 1:2.000.0000.

The region of the Persian Gulf is often subject to accidents that cause oil spills at sea, due to the richness of hydrocarbon deposits and the consequent maritime traffic; it is counted that in 2017 alone over 13,000 km^2 were spilled [2]. The event under consideration took place south of the island of Siri, in the Iranian sector of the Gulf (Fig. 1), in the first half of March 2017 when an emergency discharge occurred from the oil platform of the Siri-E field [2]. The non-profit environmental monitoring committee SkyTruth watchdog processed the SAR satellite images via the geospatial cloud platform GeoMixer, developed by Scanex, declaring that 300 to 620 m^3 of oil and / or petroleum products were spilled into the sea [2].

2.2 Dataset

The images used to study this event come from the Sentinel-1A satellite. The data used in this study are Single Look Complex (SLC) and Ground Range Detected (GRD) type belonging to Level-1 [9]. Just to get a complete idea of the actions performed on satellite data, it was decided to use SLC images in addition to the more usual GRDs as these undergo a different pre-processing with unknown parameters which, in some cases, can lead to conclusions not very exact [10]. The satellite images used for this study were acquired free of charge through NASA's Alaska Satellite Facility Data Search (ASF) portal. It was decided to use the image acquired on 12/02/17 for the image prior to the event. Instead, we chose to use the images acquired on 11/03/17 for the Change Detection procedures and those acquired on 08/03/17 for coherence estimation, given that the latter present a perfect overlap with the images of 02/12/17, a necessary condition to implement the interferometric process from which to obtain the coherence parameter. To operate through SNAP's Oil Spill tool, only the GRD-type post-event image acquired on 11/03/2017 was chosen.

2.3 Pre-processing

Images downloaded from the ASF portal require preprocessing actions. The SNAP software contains all Toolboxes for pre-processing and analysing all types of Sentinel data. Below is the list and description of the pre-processing procedures that were carried out on the SLC and GRD images (Fig. 2).

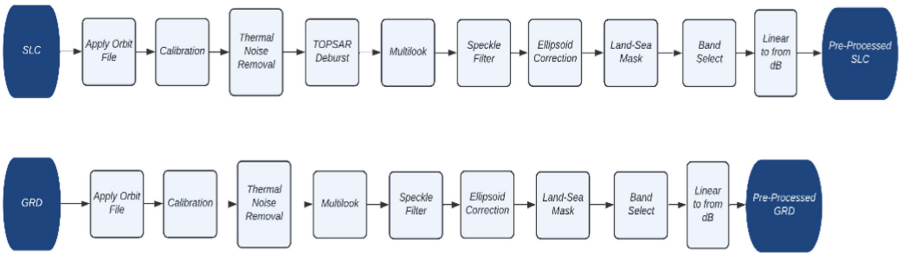


Fig. 2. SLC and GRD preprocessing workflow.

SAR products require a state orbital vector to correct spatial position accuracy. This information is present in externally hosted files, which need to be downloaded separately and are used by SNAP to update the product metadata. The Apply Orbit File process automatically downloads the OSV file and updates the metadata [12]. The objective of SAR calibration is to provide imagery in which the pixel values can be directly related to the radar backscatter of the scene. To do this, the output scaling applied by the processor must be undone and the desired scaling must be reintroduced. The radiometric scale allowed for different images by type of sensor, time and geometry of acquisition [12]. The intensity of a SAR image can be modified by the additive thermal noise. ESA provides calibrated noise vectors to subtract the power of the noise. The thermal correction of the noise can be carried out on SLC and GRD products that have not already been corrected, using a module that reduces the amount of noise from the intensity channel. The noise correction is then applied to the complex data in order to estimate the noise-free matrix [12]. TOPSAR is a progressive terrain scanning methodology performed by SAR devices; the data is acquired in bursts, then switching the antenna beam with multiple adjacent sub-bands. A product acquired with IW mode will have 3 swaths, one in EW mode will have 5. The Debursting operation merges the adjacent bursts, returning a single image by exploiting the azimuthal superposition of the individual bursts. For a GRD image, this operation has already been carried out in all the processes to obtain it starting from an SLC type image [13]. An SLC type image is acquired with a resolution ranging from 1.5×3.6 m to 2.3×14.1 m. To obtain an acquisition with a square pixel, we carry out a multilooking process of a square-sized pixel. The processing can be generated by calculating the average resolution, along the range direction or the azimuth direction, degrading the image quality but obtaining square pixels. Generally, a SAR image appears stained by the "salt and pepper noise", typical of all images of digital origin. To reduce the presence of this effect, different images are combined inconsistently, as if they correspond to different acquisitions of the same scene. Multilooking can also be used to produce an image with a reduced Speckle effect. [7]. The Speckle effect is caused by a casual constructive and destructive interference that is formed in the acquired image and which consequently forms the "salt and pepper noise". Speckle filters can be used to reduce the amount of Speckle at the cost of reduced resolution and blur. The SNAP software provides different types of Speckle filters, a Lee Sigma filter with a Windows Size 7×7 was used in our work [12]. Due to topographical variations of a scene and the tilt of the satellite sensor, distances can be distorted in the SAR images. Image data not directly at the sensor's Nadir location will have some distortion. Terrain Corrections and Ellipsoid Corrections are intended to compensate for geometric distortions caused by topography and visible in the scene as shadows, foreshortening, and layovers. The result is an image that is closer to the reality of the territory. Since our study area falls into the sea, it is advisable to use the ellipsoidal one as a reference surface and therefore we use the Ellipsoid Correction operator [14]. The Land-Sea Mask operator allows you to make a split between the part of the image occupied by land and that occupied by an aquatic mirror. This operation has the double utility of avoiding the presence of a disturbing action in the analysis which can lead to false positives. Furthermore, by eliminating the part of the soil that is not of interest for this study, we reduce the computational load that aggravates on the device used for the processing. This operation is carried out

through the automatic download of a DEM that immediately recognizes the height of each pixel and is therefore able to deduce whether it is on the mainland or not [14]. The conversion from Digital Number to decibel transforms the backscatter intensity into a more user-friendly quantity, with a better degree of visibility and, generally, accepted as a unit of measurement for a given radar [15]. The Band Select operation is used to select the band on which we want to carry out the conversion operation (VV). At the end of the pre-processing operations we obtain, both for the SLC and GRD image, a product with the optimal characteristics for the processing required for the actual processing (Figs. 3 and 4).

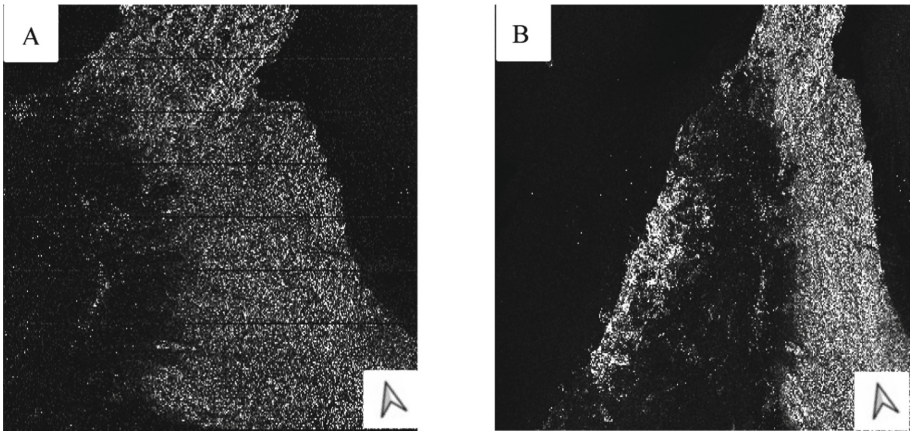


Fig. 3. SLC image before pre-processing, Scale 1:580.000 (A); GRD image before pre-processing, Scale 1:1000.000 (B).

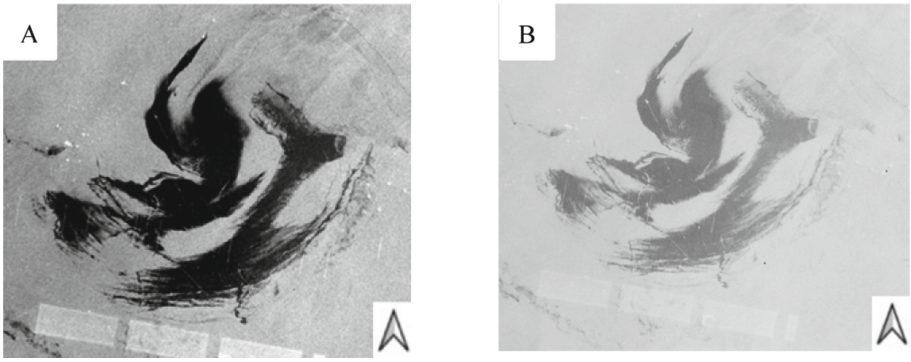


Fig. 4. SLC image after pre-processing (A); GRD image after pre-processing (B). Scale 1: 250.000.

2.4 Processing

Once the pre-processing of the images is finished, it is possible to move on to the actual processing that allowed us to achieve the originally set goals. The processing performed involves an initial phase of co-registration of the pre and post event images, the application of a smoothing filter and finally a calculation operation between the backscatter values of the two images through a mathematical expression.

Co-registration

The first step is to carry out a co-registration of the sub-pixels of the SAR images, a fundamental requirement for carrying out any comparison operation [16]. The result to be obtained through this step is to spatially align the two images so that the characteristics of a reference image are superimposed on those of the image to which the first is coupled, to be able to make a comparison as accurate as possible [17].

Co-registration is normally done by selecting an image as the reference (master) to which all other images are aligned [13]. The co-registration process requires the identification of common characteristics between the master and the slaves and the subsequent adaptation of the slaves to the master. The positions of the common features are called "Tie points" and are used by the co-registration application as a reference. Once enough binding points are generated, a polynomial function is used to align the deformed slave image to the master [17].

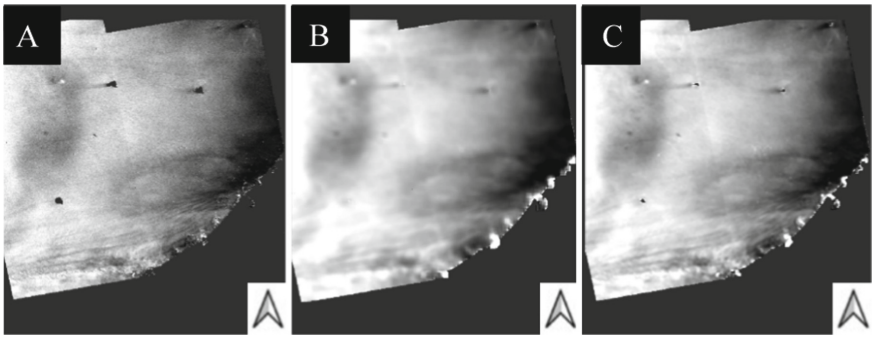


Fig. 5. Pre-event image respectively without smoothing filter (A), with 10 × 10 pixels kernel smoothing (B), with 20 × 20 pixels kernel smoothing (C). Scale 1: 800.000

Smoothing

In some of the previous elaborations the problem of video noise emerged, something common in the field of remote sensing. When it comes to detecting edges and edges, noise in images greatly affects detection accuracy; therefore, controlling the intensity of the pixel values helps the model in use to focus on general details and obtain greater precision [18]. By smoothing, we reduce the high-frequency details: the back-scatter value of each pixel is defined according to mathematical relationships with those of the backscatter of the pixels surrounding it within a kernel of a fixed size [19]. By increasing

the kernel size, we increase the smoothing, thus obtaining different results; it is therefore advisable to carry out a good calibration of the values used during the procedure. Among the various mathematical filtering relationships, the choice fell on the median blurring, which averages all the pixels belonging to the same kernel and replaces the values of all the pixels with the one calculated in the kernel [20]. This filter was used exclusively on the image depicting the pre-event, to further reduce the "salt and pepper noise" caused by the irregularity of the sea surface. In our work the effects of kernels of 10 × 10 pixels and 20 × 20 pixels size were evaluated (Fig. 5).

2.5 Change Detection Analysis and Threshold Values Definition

We can define the Change Detection operation as the process that identifies the differences in the properties of an object by observing it at different instants of time [21]. The comparison is made between the image acquired prior to the event, on February 12, 2017, and that acquired in conjunction with the event, on March 11, 2017. The determination of the threshold value subsequently used as part of the Change Detection was carried out by calculating the difference of the average backscatter value of the pixels that contain the oil stain in the post-event image and the average value of the unstained ones in the pre-event image. The irregular and jagged nature of the patch did not allow to define in a precise, simple, and rapid way the average backscatter value assumed by the stained pixels and that assumed by the non-stained pixels. Not being able to use simple geometries as useful polygons to define homogeneous areas, we opted for an analysis by sections. Initially, within the image containing the oil spill, a backscatter value was determined that was able to discern the presence or less of oil by tracing Sect. 1 totally falling within the oil and Sect. 2 falling totally in the water (Fig. 6). Plotting the results, the values shown in Table 1 were obtained.

Table 1. Backscatter values in the post-event image for sections 1 and 2.

Backscatter Section 1 (oil) (dB)	
Maximum value	−28.85
Maximum value	−31.91
Average value	−30.54
Backscatter Section 2 (water) (dB)	
Maximum value	−21.11
Maximum value	−23.42
Average value	−22.26

A value of −25 dB was therefore chosen to assign or not the status of "spot-to" to the pixel in question, as the maximum value of a pixel falling within the oil spot is well below this value; conversely, an "unstained" pixel has backscatter values well above the value we have designated. Once the water-oil discriminating value had been determined,

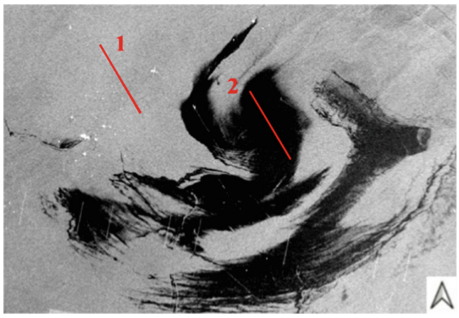


Fig. 6. Sections 1 and 2 used to determine the oil-water discriminant backscatter value. Scale 1: 200.000.

it was possible to move on to the study of Sects. 3 to 6 which cross both floating oil and the sea without it and therefore with heterogeneous backscatter values (Fig. 7). In the post-event image, for each section, the pixels with backscatter values lower than −25 dB, in which the presence of hydrocarbons was detected, were separated from those with higher values, which were considered free from the same hydrocarbons, by calculating the average of the values of the two parts. In the pre-event image, the average backscatter value was calculated along the section uniformly made up of water. The threshold value of each section was therefore defined as the difference between the average backscatter value of the oil pixels in the post-event image and the average backscatter value of the water pixels in the pre-event image. This operation made it possible to obtain four threshold values; finally, the average of these four values allowed to obtain the threshold value which was subsequently used in the Change Detection calculations. The average threshold values of each section, both for SLC and GRD images, are shown in Table 2.

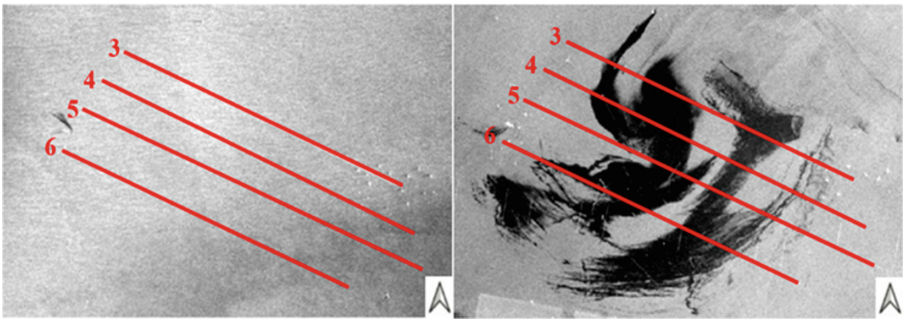


Fig. 7. Sections used to determine the Threshold value. Scale 1: 200.000.

In addition to the values determined by this procedure, it was decided to repeat the Change Detection operation also for threshold values close to the excess and defect values calculated, such as −12.5 dB, −13 dB and −14 dB. The smoothing operation was carried out exclusively for the Change Detection in which the calculated average threshold value was used. The subtraction between the backscatter values of the master image and those

Table 2. Average Threshold values calculated for SLC (left) and GRD (right).

Threshold SLC (dB)		Threshold GRD (dB)	
Section 1	13.89	Section 1	13.78
Section 2	12.96	Section 2	14.85
Section 3	13.50	Section 3	13.90
Section 4	12.67	Section 4	14.67
Average Value	13.26	Average Value	14.30

of the slave image was done through the "Band Math" operator. Subsequently, a binary mask was created composed exclusively of pixels having a threshold equal to or greater than the values we have chosen. The raster containing the mask was then exported and processed using the QGIS software. Within the latter, a vectorization operation was carried out and a Sieve Classification was subsequently carried out using the Semi-Automatic Classification Plugin tool. Sieve Classification is a procedure that allows you to replace the value of the isolated pixels with that of the surrounding pixels. This procedure is useful for removing isolated parts from the classification [22]. Finally, using the Field Calculator tool, the total area occupied by oil was calculated as the sum of the areas of the remaining polygons.

2.6 Oil Spill Detection Tool

Inside the SNAP software there is the "Oil Spill Detection" tool based on an algorithm that can be used for detecting oil spills [23]. This tool was created by training on a set of images coming from the waters of the northern European seas; generally, it performs good results, except for the presence of several false positives, caused using an adaptive algorithm for calculating the threshold based on a single image and not on a Change Detection [23]. The operator follows the following operations: a pre-processing phase, in which a calibration is performed and a Speckle filter is applied; a phase of Land-sea masking which serves to focus the detection exclusively on the area concerned; a phase of Dark Spot detection, in which dark spots are identified using the adaptive algorithm; finally a Clustering and Discrimination phase in which the identified pixels are collected in clusters or eliminated on the basis of the minimum size chosen for cluster formation [24]. The Adaptive Threshold Algorithm works by finding an average local backscatter, using a comparison kernel size chosen by the user; after which the software discriminates the spots that have a backscatter lower than the average local one as "smudged". This algorithm performs best with Radarsat and ENVISAT SAR images, for which a training activity was carried out [14]. With respect to the case in question, the image acquired on 11/03/17 was processed, to make a direct comparison with the results of the Change Detection process, for which the same data was used. The output of the process, produced after a processing time of several hours, is a raster image in which the pixels recognized as "stained" are displayed, aggregated in clusters.

2.7 Thickness Value Used to Calculate the Volumes

After having completed the processing that allowed the determination of the spilled hydrocarbon surface, it was possible to calculate the corresponding volume. To obtain this result, an estimate of the thickness that this fluid can occupy in the sea was considered. The exact determination of this parameter is very complex as it depends on various factors such as, for example, the type of hydrocarbon itself, its temperature, sea temperature, etc. [25]. Furthermore, the possibility of aggregating or not of the spilled fluid, in order to form the easily distinguishable "dark patches", depends very much on the meteorological conditions: the movement of oil is very susceptible to wind and surface currents, which can move it on the water surface and disperse it [26]. In the case of optical images, it is possible to perform a colorimetric analysis that makes a corresponding thickness correspond to a certain colour, which will therefore be spatially variable [27]. In the case of SAR images, it is not possible to carry out this type of analysis because it is not possible to appreciate the spectral characteristics that make the patch assume different colours. However, we can start from the consideration that to be detected by a SAR, a hydrocarbon must have a thickness of at least one micron [25]; starting from this assumption it was possible to make an indicative estimate of the volume of floating oil.

2.8 Coherence Estimation

The local coherence of two radar satellite images is defined as the correlation coefficient obtained by crossing two SAR images and making the ratio between the coherent and inconsistent summations calculated for each point. The value of Coherence C goes from 0 to 1; for values close to 1 we will have to deal with highly coherent pixels, typical behaviour of built structures or rocky areas, which undergo minimal change over time; for values close to 0 we will have a low coherence content, a typical behaviour of changing elements such as vegetal or aquatic ones [28]. After applying the Orbit file, a splitting operation of the SLC image was carried out. The Back Geocoding operator made it possible to co-register the two previously split SLC images. Following the co-registration of the two satellite images, the Network Enhanced Spectral Diversity (NESD) was used to estimate the azimuth shift between the radar images, to minimize the phase discontinuities between the different bursts. Then a Deburst is performed to merge the different bursts and obtain a unique Coherence image. Finally, to refine the image quality, a multilooking operation is performed, to return a square dimension to the pixel and reduce the Speckle, and an ellipsoidal correction to eliminate the deviation between the geoid and the reference ellipsoid. At the end of the processing, we moved on to the evaluation of the Coherence values: initially the Coherence values were analysed using sections that crossed the oil stain. This methodology, due to the prevailing inconsistent nature of the sea, within the scene, did not yield useful results for the purposes of our research. Given this, later, geometries were built, externally and internally to the spot displayed in the reference image, and the differences between the average values of coherence calculated inside the spot and outside were measured; the comparison was made both by means of means and by means of the ninetieth percentile.

2.9 WebGNOME

The catastrophic consequences caused by an Oil Spill event [29] have led, over the years, to the need to refine the techniques for identifying and detecting spills [30]. However, it was also necessary to develop techniques that would make it possible to reconstruct the dynamics of the accident and to predict its spread and future evolution. To meet this need, (NOAA) has developed a software, WebGNOME, equipped with a model capable of elaborating the path that the spilled hydrocarbon can follow, both from a chemical and physical point of view, based on how the latter is influenced by the atmospheric and morphological conditions of the analysed case [8].

Dataset
WebGNOME can be used by entering various data sources: the map, the wind and sea currents, the diffusion parameters, the temperature, the salinity, the type of hydrocarbon, the type and duration of Spill [8]. A spill phase duration of 3 days was set, for a total of 401,000 spilled gallons (data calibrated to obtain a quantity of floating material equal to that detected). The type of hydrocarbon chosen, in the list made available by the ADIOS Oil Database, corresponds to "DUBAI, OIL & GAS", with an API gravity equal to 31.081 and a Pour point equal to −9.0 °C. The water temperature [31] was set to 21.9 °C [32], the salinity equal to 32 psu [33] and the Sedimentation Load equal to 5 mg/l [33]. The horizontal diffusion coefficient was set to a value equal to 1e + 5 cm^2/s [34]. The wind was set for intensity and direction with a variability of six hours between one measurement and another. Finally, the currents were obtained from the GOODS website, made available by NOAA, from which it is possible to download the files necessary to correctly set the trend of the sea currents within the model [35]. The duration of the simulation was set at 6 days and 3 h, to make the end of the simulation coincide with the moment in which the post-event image used in the study was recorded.

Processing
The spilled hydrocarbon is modelled by the software through points with mass that the program calls "Lagrangian Elements" or "LE". Each LE has its location, release time, age, type of pollution and status (floating, beached or evaporated) [8]. In WebGNOME the diffusion of material is treated as a stochastic process; the effects of gravity and surface tension are ignored, because they only affect the first instants of spill. The model uses a classic diffusion equation, here expressed in Cartesian coordinates:

$$\frac{\partial C}{\partial t} = D_x * \frac{\partial^2 C}{\partial x^2} + D_y * \frac{\partial^2 C}{\partial y^2} \tag{1}$$

where C is the concentration of the material and D is the diffusion coefficient. The movement of each element is calculated moment by moment, vectorially adding the intensity transmitted by the wind and that transmitted by the current. The movement caused by the current is calculated through an algorithm called Directional Acyclic Graph (DAG) Tree, who divides the map into triangles and calculates, for each particle inside the triangle itself, on which of the adjacent triangles there is more probability that the particle moves. This procedure makes it possible to greatly lighten the complexity of the calculation with respect to the methodologies that are based on the nearest neighbour

for each specific element. The Windage data entered is interpolated through a Hermite polynomial; subsequently the consequent wave motion generated is calculated from the intensity of the wind, mainly responsible for the motion of the oil particles [36]. Recent studies relating to the prediction of wave motion using neural networks could prove useful for the evolution of the oil diffusion model [39, 40]. Furthermore, for the calculation of evaporation and sedimentation, WebGNOME uses a three-phase calculation algorithm, based on the model developed by Boehm, Feist, Mackay, & Paterson [37]. Two types of solutions are obtained through the software: a "best estimate solution" and a "minimum regret solution". The "best estimate", the one chosen in this paper, considers only the Lagrangian Elements whose movement, according to the calculations made by the software, is deemed correct with excellent probability; the "mini-mum regret", on the other hand, also considers a certain uncertainty in the input data, to which a variable and uncertain output data will correspond, which contemplates within it a wider but at the same time more uncertain set of diffusion possibilities; the latter methodology is useful for determining the "worst case scenario" [8]. By using WebGNOME it was possible to validate the detection carried out via satellite image, verifying the actual matching between the spot extrapolated through the SNAP program and the one obtained from the web software calculations. Parallel to the analysis concerning the movement and diffusion of the pollutant, the WebGNOME software also performs a chemical analysis of each individual Lagrangian element. The component of the program that carries out this analysis is the Automated Data Inquiry for Oil Spills (ADIOS); this tool models oil spills to analyse physico-chemical changes [38]. Using ADIOS it was therefore possible to reconstruct, starting from the quantity of floating hydrocarbon identified by the satellite image, the sedimented quantity, that naturally dispersed and that evaporated and, consequently, also the total volume that characterized the accident in its entirety.

3 Results and Discussion

The oil surfaces obtained from the analysis carried out through Change Detection (Fig. 8) and the volumes obtained considering the thickness of one micron are collected in Table 3. The reference volume is that determined by the SkyTruth portal equal to 163876 gallons.

The Table 3 first distinguishes the results obtained for the SLC and GRD images; the threshold values used, the possible size of the Smoothing kernel, the calculated volume expressed in gallons and the percentage difference in absolute value from the comparison measure are also indicated. It is possible to notice a discrepancy between the results obtained starting from an SLC image compared to those obtained from a GRD. The result obtained using the threshold value obtained through the section method, has a percentage discrepancy with respect to the reference volume ranging from 6.7% to 6.9% as regards the SLC, of 5.5% for the GRD image. We can therefore note how the application of the Smoothing filter has a negligible contribution to the result, causing the result to vary by 0.2% in the SLC and by a value of less than 0.1% for the GRD. By carrying out the Classification Sieve process on the SLC image with a difference value equal to −13.258 with no smoothing, while obtaining a cleaner image, there is a loss of information which leads to an increase, even if minimum, of the deviation from the reference measure,

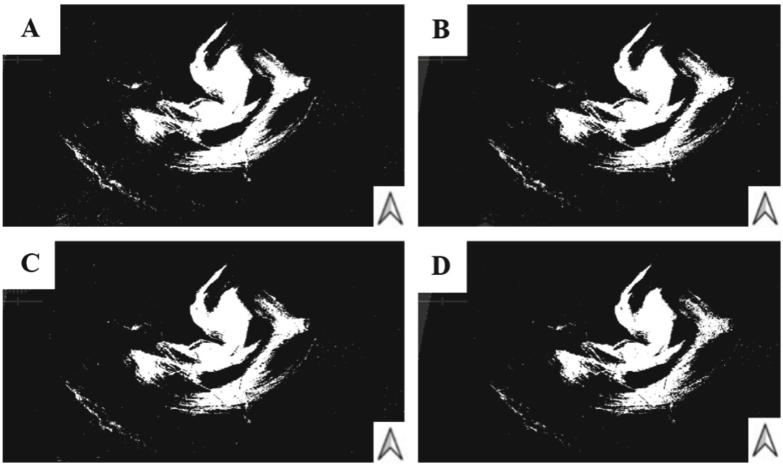


Fig. 8. Resulting images of the Change Detection process respectively with Threshold values equal to −12.5 dB (A), −13 dB (B), −13.258 dB (C), −14 dB (D). Scale 1: 55.000.

Table 3. Volume Analytics.

Declared Volume = 163876 gal				
Threshold (dB)	Smoothing filter (Pixel)	Sieve filter	Computed volume (gal)	Variation (%)
Change Detection SLC				
Difference - 12.5	NO	NO	169762.5	3.59%
Difference - 13	NO	NO	158388.0	−3.35%
Difference - 13.258	NO	NO	152911.2	−6.69%
Difference - 13.258	10	NO	152960.1	−6.66%
Difference - 13.258	20	NO	152604.0	−6.88%
Difference - 13.258	NO	YES	152624.8	−7.00%
Difference - 14	NO	NO	137349.9	−16.19%
Change Detection GRD				
Difference - 12.5	NO	NO	181226.7	10.59%
Difference - 13	NO	NO	160971.1	−1.77%
Difference - 14.301	NO	NO	154913.0	−5.47%
Difference - 14.301	10	NO	154920.6	−5.46%
Difference - 14.301	20	NO	154818.7	−5.53%
Difference -15	NO	NO	140120.0	−14.50%
SNAP Oil Spill tool				
Undefined	NO	NO	137728.4	−15.96%



Fig. 9. Resulting image of the single image Oil Spill Tool integrated into SNAP. Scale 1: 200.000.

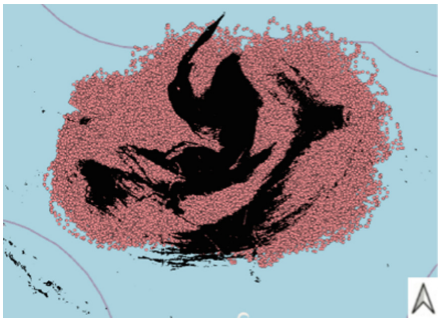


Fig. 10. Comparison between the spot detected by Change Detection in SNAP and Lagrangian Elements from WebGNOME. Scale 1: 200.000.

advising against its use for the purpose of a precise volumetric analysis. The best values will be obtained with a threshold value slightly lower than that calculated by us which therefore tends to undersea the actual volume value by 3–4%. The recognition obtained through the tool integrated in the single image "Oil Spill Tool" program (Fig. 9) leads to a difference of 16%, which indicates the inadequacy of the methodology in the exact recognition of the quantities spilled, moving us away by more than ten percentage points from the optimal measurements obtained from our studies. Analysing the results obtained through the Coherence Estimation procedure, it is noted that no significant and useful results emerge for the analysis: the changing nature of the aqueous medium does not lend itself, at a macroscopic level, to an interferometric analysis which allows to obtain appreciable coherence results. By examining the numerical results obtained from the coherence analysis of a geometry falling within the oil stain and comparing them with those of a geometry not falling within the stain, we obtain a deviation between the percentages of -1.5% compared to the average value and -2.2% as regards the 90th percentile. From the visual comparison between the stain detected through the SNAP procedures and that calculated through the dynamic model WebGNOME (Fig. 10) it can be seen how the two procedures, carried out in parallel, lead to a good overlap of results: the spill obtained from the satellite images it is in fact almost entirely incorporated in the cloud of points that the software developed by NOAA generates. The use of WebGNOME is therefore, from our studies, valid in predicting the behaviour of the spilled hydrocarbon, restricting the field of investigation in which cleaning operations could be carried out. In addition, this procedure allows you to reconstruct the origin and mode of diffusion of the fluid, possibly allowing you to investigate the causes; this problem is widespread in the field of detecting oil spills as it is often difficult to reconstruct the dynamics of accidents due to the unavailability of information. In this sense, the use of the ADIOS tool, which is part of the WebGNOME package, is also useful: this tool performs a chemical analysis, based on the data entered in the model,

from which it obtains, moment by moment, the hydrocarbon values evaporated, naturally dispersed, settled and floating. The floating material, in the case under consideration, constitutes only 40.8% of the total volume spilled. Starting from this data it was possible to trace a quantity of spilled volume equal to 401000 gallons (Fig. 11).

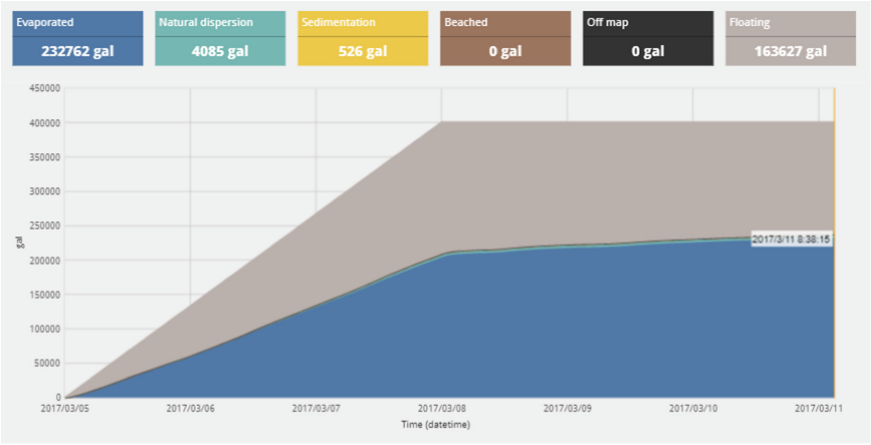


Fig. 11. Reconstruction of the event carried out using the ADIOS software.

4 Conclusions

The outputs obtained from the study confirm that more truthful results can be obtained in the identification and subsequent estimation of the mass of spilled hydrocarbons through a Change Detection process both on an SLC-type image and on an image of the GRD compared to the procedures that analyse a single image, such as the one performed by the Oil Spill Tool integrated in SNAP. The values are however affected by a degree of inaccuracy because in a SAR image it is not possible to appreciate the different densities that oil can assume in the act of floating on an aquatic surface. In this regard, it may be useful to carry out a more in-depth comparison with Change Detection procedures that have an optical type of image as the object of study, such as that obtained from Sentinel-2 satellites. The procedure used to determine the threshold value is confirmed to be suitable for recognizing an Oil Spill having given results close to those found in literature: this result could be further improved by reducing the random component that this type of measurement brings with it, by increasing the number and size of the sections used. The Coherence analysis carried out did not lead to decisive results: this is because the sea surface has a changing nature that does not lend itself well to the type of research carried out and does not give appreciable macroscopic results. This kind of procedure could therefore be more effective for the analysis of an Oil Spill phenomenon that does not occur in the marine environment but on land. The WebGNOME software was used as a validation tool for the survey carried out via satellite image; the good overlap between the results of the two models testifies to the correctness of the model and the

possibility of its use for validation procedures, reconstruction of the Oil Spill event and its environmental consequences, thanks to the chemical-physical analysis performed by the ADIOS tool. For this purpose, the component of the imputed meteorological data, the type of spilled hydrocarbon and the spillage method are of particular importance for the correct functioning; to increase the reliability of the generated model, it will therefore be appropriate to improve the quality and quantity of the input data that describe the actual conditions in which the event takes place.

References

1. Cervelli, E., Pindozzi, S., Capolupo, A., Okello, C., Rigillo, M., Boccia, L.: Ecosystem services and bioremediation of polluted areas. Ecol. Eng. **87,** 139–149 (2016)
2. Scanex Satellite monitoring of oil pollution in the Persian Gulf. https://www.scanex.ru. Accessed 16 Mar 2022
3. Fingas, M., Brown, C.: Review of oil spill remote sensing. Mar. Pollut. Bull. **83**(1), 9–23 (2014)
4. Capolupo, A., Pindozzi, S., Okello, C., Fiorentino, N., Boccia, L.: Photogrammetry for environmental monitoring: the use of drones and hydrological models for detection of soil contaminated by copper. Sci. Total Environ. **514**, 298–306 (2015)
5. Capolupo, A., Pindozzi, S., Okello, C., Boccia, L.: Indirect field technology for detecting areas object of illegal spills harmful to human health: application of drones, photogrammetry and hydrological models. Geospat. Health **8**(3), S699–S707 (2014)
6. Capolupo, A., Nasta, P., Palladino, M., Cervelli, E., Boccia, L., Romano, N.: Assessing the ability of hybrid poplar for in-situ phytoextraction of cadmium by using UAV-photogrammetry and 3D flow simulator. Int. J. Remote Sens. **39**(15–16), 5175–5194 (2018)
7. Fan, J., Zhang, F., Zhao, D., Wang, J.: Oil spill monitoring based on SAR remote sensing imagery. Aquatic Procedia **3**, 112–118 (2015)
8. Beegle-Krause, J.: General NOAA oil modeling environment (GNOME): a new spill trajectory model. In: International oil Spill Conference, vol. 2001, No. 2. American Petroleum Institute (2001)
9. ESA Mission Sentinel-1. https://www.esa.int. Accessed 01 Mar 2022
10. Potin, P.: Sentinel-1 mission overview (2011)
11. Prats-Iraola, P., et sl.: Sentinel-1 assessment of the interferometric wide-swath mode. In: 2015 IEEE international geoscience and remote sensing symposium (IGARSS). IEEE (2015)
12. Filipponi, F.: Sentinel-1 GRD preprocessing workflow. Multidisciplinary digital publishing institute proceedings, vol. 18. No. 1 (2019)
13. Veci, L., Lu, J., Foumelis, M., and Engdahl, M.: ESA's Multi-mission Sentinel-1 Toolbox. In: EGU General Assembly Conference Abstracts (2017)
14. Prastyani, R., Abdul, B.: Utilisation of Sentinel-1 SAR imagery for oil spill mapping: a case study of Balikpapan Bay oil spill. J. Geospatial Inf. Sci. Eng. **1**(1) (2018)
15. Nasirzadehdizaji, R., Cakir, Z., Sanli, F.B., Abdikan, S., Pepe, A., Calò, F.: Sentinel-1 interferometric coherence and backscattering analysis for crop monitoring. Comput. Electron. Agric. **185**, 106118 (2021)
16. Mandal, D., Vaka, D.S., Bhogapurapu, N.R., Vanama, V.S.K., Kumar, V., Rao, Y.S., Bhattacharya, A.: Sentinel-1 SLC preprocessing workflow for polarimetric applications: a generic practice for generating dual-pol covariance matrix elements in SNAP S-1 toolbox (2019)
17. Usman, F., Nanda, N., Nasmirayanti, R., Sumantyo, J.T.S.: Comparative analysis on digital surface model of urban area from Sentinel-1 SAR interferometry and aerial photogrammetry for disaster mitigation plan. In E3S Web of Conferences, vol. 331, p. 04017. EDP Sciences (2021)

18. Ali, I., Cao, S., Naeimi, V., Paulik, C., Wagner, W.: Methods to remove the border noise from Sentinel-1 synthetic aperture radar data: implications and importance for time-series analysis. IEEE J. Sel. Top. Appl. Earth Observ. Remote Sensing **11**(3), 777–786 (2018)
19. Kumari, M., Murthy, C.S., Pandey, V., Bairagi, G.D.: Soybean cropland mapping using multi-temporal SENTINEL-1 data. International Archives of the Photogrammetry, Remote Sensing & Spatial Information Sciences (2019)
20. Indriasari, N., et al.: Analisa filter spekle single dan multitemporal data Sentinel 1-A. In: IOP Conference Series: Earth and Environmental Science, vol. 500. No. 1. IOP Publishing (2020)
21. Turgay, C.: Change detection in satellite images using a genetic algorithm approach. IEEE Geosci. Remote Sens. Lett. **7**(2), 386–390 (2010)
22. Al-Ahmadi, F.S., Al-Hames, A.S.: Comparison of four classification methods to extract land use and land cover from raw satellite images for some remote arid areas, Kingdom of Saudi Arabia. Earth Sci. **20**(1) (2009)
23. Misra, A., Balaji, R.: Simple approaches to oil spill detection using sentinel application platform (SNAP)-ocean application tools and texture analysis: a comparative study. J. Indian Soc. Remote Sens, **45**(6) (2017)
24. Capizzi, G., Sciuto, G.L., Woźniak, M., Damaševicius, R.: A clustering based system for automated oil spill detection by satellite remote sensing. In: International Conference on Artificial Intelligence and Soft Computing. Springer, Cham (2016)
25. Prasad, S.J., Balakrishnan Nair, T.M.: Quantification of oil lost from tanker vessel using space borne radar datasets-Case study of Haldia port oil spill. In: International Oil Spill Conference. vol. 2021. No. 1, July 2018 (2021)
26. Dąbrowska, E., Kołowrocki, K.: Hydro-meteorological change process impact on oil spill domain movement at sea. In: Zamojski, W., Mazurkiewicz, J., Sugier, J., Walkowiak, T., Kacprzyk, J. (eds) Theory and Applications of Dependable Computer Systems. DepCoS-RELCOMEX 2020. Advances in Intelligent Systems and Computing, vol. 1173. Springer, Cham. https://doi.org/10.1007/978-3-030-48256-5_17
27. Fingas, M.: The challenges of remotely measuring oil slick thickness. Remote Sens. **10**(2), 319 (2018)
28. Touzi, R., Lopes, A., Bruniquel, J., Vachon, P.W.: Coherence estimation for SAR imagery. IEEE Trans. Geosci. Remote Sens. **37**(1), 135–149 (1999)
29. Palladino, M., Nasta, P., Capolupo, A., Romano, N.: Monitoring and modelling the role of phytoremediation to mitigate non-point source cadmium pollution and groundwater contamination at field scale. Ital. J. Agron. **13**.s1 (2018)
30. D'Andrea, M. A., and G. Reddy, K.: Health consequences among subjects involved in Gulf oil spill clean-up activities. Am. J. Med. **126**(11), 966–974 (2013)
31. Tarantino, E.: Monitoring spatial and temporal distribution of Sea Surface Temperature with TIR sensor data. Italian J. Remote Sensing/Rivista Italiana di Telerilevamento **44**(1) (2012)
32. Noori, R., et al.: Recent and future trends in sea surface temperature across the Persian Gulf and Gulf of Oman. PloS one **14**(2), e0212790 (2019)
33. Dubach, H.W.: A Summary of temperature-salinity characteristics of the persian gulf. National oceanographic data center Washington D.C. (1964)
34. Al-Ghadban, A.N., Abdali, F., Massoud, M.S.: Sedimentation rate and bioturbation in the Arabian Gulf. Environ. Int. **24**, 1–2 (1998)
35. Samuels, W.B., Amstutz, D.E., Bahadur, R., Ziemniak, C.: Development of a global oil spill modeling system. Earth Sci. Res. **2**(2), 52 (2013)
36. Zelenke, B., O'Connor, C., Barker, C.H., Beegle-Krause, C.J., Eclipse, L.: General NOAA operational modeling environment (GNOME) technical documentation (2012)
37. Jung, T.H., Son, S.: Oil spill simulation by coupling three-dimensional hydrodynamic model and oil spill model. J. Ocean Eng. Technol. **32**(6), 474–484 (2018)

38. Elizaryev, A., et al.: Numerical simulation of oil spills based on the GNOME and ADIOS. Int. J. Eng. Technol. (UAE) **7**(2), 24 (2018)
39. Sadeghifar, T., Lama, G.F.C., Sihag, P., Bayram, A., Kisi, O.: Wave height predictions in complex sea flows through soft-computing models: case study of Persian Gulf. Ocean Eng. **245**, 110467 (2022)
40. Lama, G.F.C., Sadeghifar, T., Azad, M.T., Sihag, P., Kisi, O.: On the indirect estimation of wind wave heights over the Southern Coasts of Caspian Sea: a comparative analysis. Water **14**(6), 843 (2022)